

Electronic Supplementary Information for:

From graphene to graphene oxide: the importance of extended topological defects

*Alexander J. Marsden[§], Mark Skilbeck[§], Matthew Healey[§], Helen R Thomas[‡], Marc Walker[§],
Rachel S. Edwards[§], Natalya A. Garcia[×], Filip Vuković[×], Hicham Jabraoui[×], Tiffany R.
Walsh[×], Jonathan P Rourke[‡], Neil R. Wilson[§]*

[§]Department of Physics and [‡]Department of Chemistry, University of Warwick, Coventry,
CV4 7AL, U.K.

[×]Institute for Frontier Materials, Deakin University, Geelong VIC, 3216, Australia

Table of Contents

<i>ESI1: XPS and Raman spectroscopy of CVD graphene after dosing with atomic oxygen....</i>	2
<i>ESI2: Selected area electron diffraction of functionalised graphene.</i>	4
<i>ESI3: Molecular Dynamics Simulations</i>	8
Model Justification	8
Figures and Tables	10
<i>ESI4: Computational Details</i>	14
Functional Group Analysis.....	15
Rendering Methods	15
Mechanical Property Calculations	16
<i>ESI5: Measuring mechanical properties by atomic force microscopy</i>	18
<i>REFERENCES:</i>	22

ESI1: XPS and Raman spectroscopy of CVD graphene after dosing with atomic oxygen.

Figure S1a shows XPS of graphene on copper after dosing with atomic oxygen. On each spectrum black points are the raw data, the red line is the cumulative fit, and the shaded regions represent individual fitting components. In the C1s region shown, there is a single asymmetric peak which can be fit with a Doniach-Sunjic asymmetric line profile¹ at 284.4 ± 0.1 eV, as often used for graphene.² After 1 minute of dosing with atomic oxygen, a symmetric peak arises at 286.3 ± 0.1 eV, corresponding to carbon in an epoxide group; this is consistent with prior work that has shown exposing graphene to atomic oxygen results in reversible on-plane functionalisation in the form of epoxide groups.^{3,4} Further dosing for 2 and 4 minutes does not introduce extra peaks but does increase the relative intensity of the epoxide peak, demonstrating the increase in the number of these functional groups as the graphene is exposed to atomic oxygen for longer times.

However, a new peak at 288.5 ± 0.1 eV is observed in the C 1s region after an 8-minute dose of atomic oxygen to graphene. Peaks at this binding energy are again associated to oxygen groups, but in carbonyl (C=O) and carboxyl (C(O)OH) environments. The peak broadness suggests a mixture of these environments, but the resolution is not sufficient to distinguish between them. For the 16-minute dosed graphene, the spectrum appears much the same. Both the 8 and 16 min dose XPS spectra resemble those of GO.

The XPS spectra show that at lower levels of functionalisation (between 1 and 4 minutes) the atomic oxygen forms epoxide groups on the graphene surface, consistent with previous reports on exposing graphene to atomic oxygen.^{3,4} For doses greater than 4 minutes there is a change in the oxygen chemical environments: the epoxides remain but are joined by carboxyl and carbonyl groups. It is worth noting that after 4 minutes the total C1s intensity starts to decrease, suggesting some removal of carbon from the surface. Combined, this evidence

points to significant disruption to the graphene lattice caused by not only higher levels of oxygen functionalisation, but also in-plane defects associated with the loss of carbon atoms.

Figure S1b shows Raman spectra from graphene before and after oxygen functionalisation. The top panel shows a Raman spectrum from pristine graphene on copper, with a single peak at 1590 cm^{-1} which can be assigned to the G band of graphene.⁵ There are no other peaks in this region, including around 1345 cm^{-1} where the D peak would be expected, indicating the graphene is free from disorder, typical for high-quality CVD graphene.

The panels below, in Figure S1b, show Raman spectra from graphene after oxygen dosing. For the 1-minute dosed graphene, the G peak is still present but, the D peak at 1345 cm^{-1} is now significant. After longer exposures to atomic oxygen, the D' peak at 1650 cm^{-1} emerges as well. Both D and D' peak are related to disorder in the graphene lattice.⁵ As the dosing increases, the D and D' peaks increase relative to the G peak, suggesting an increase in disorder in the lattice with increasing dosing. After >4 minutes exposure to atomic oxygen, the G and D' peaks become too broad to be distinguished by eye.

The bottom panel in Figure S1b shows a Raman spectrum from base-washed graphene oxide (bwGO) as a comparison. The two broad peaks at 1600 cm^{-1} and 1360 cm^{-1} , assigned to the D, and to the G and D' combined respectively, closely resemble those from 8- and 16-minute dosed graphene on copper, suggesting comparable disorder to the graphene lattice.

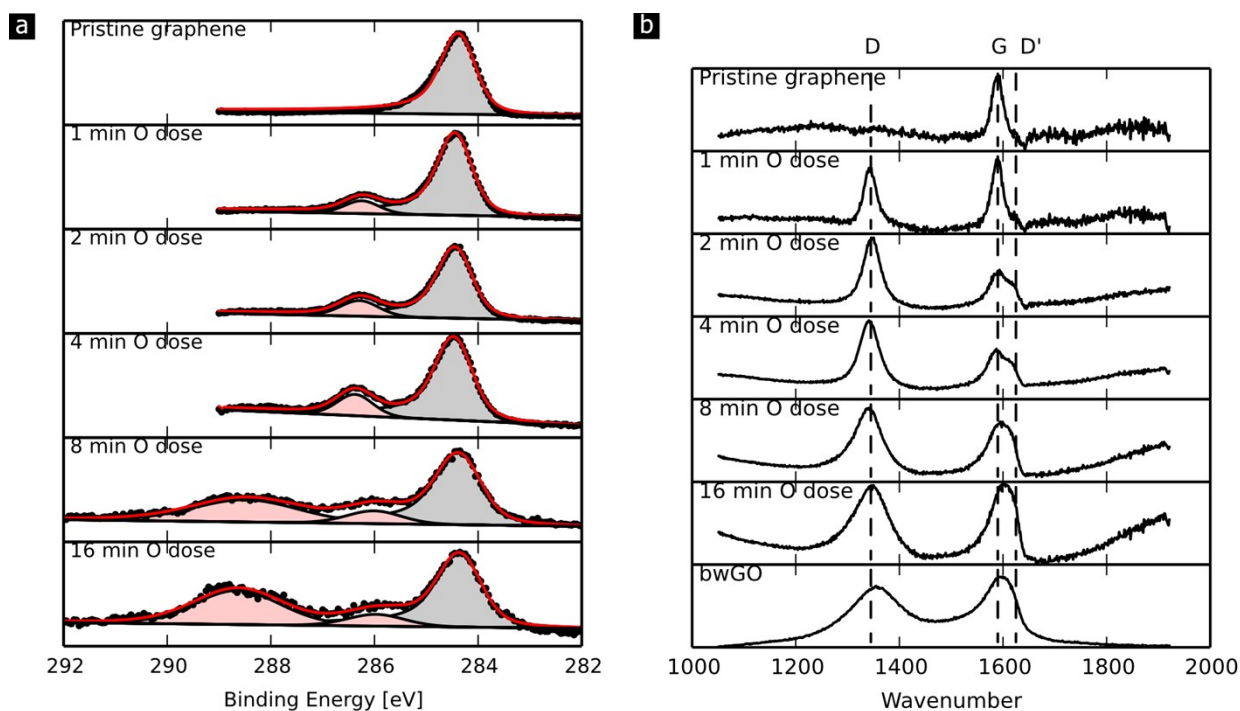


Figure S1 (as in Figure 1 of the main text). XPS and Raman spectroscopy of atomic oxygen functionalised graphene and GO. a) C1s XPS spectra for graphene with different times of exposure to atomic oxygen, the red line is the fit to the data with the fitted peaks shown as black lines with shading beneath. b) Raman spectra, the dashed lines indicate the positions of the D, G and D' peaks.

ESI2: Selected area electron diffraction of functionalised graphene.

Selected area electron diffraction patterns were acquired using a JEOL 2100 TEM operating at 200 kV: a plug-in to Digital Micrograph was used to automatically acquire a sequence of images at increasing acquisition times and combine them into a single high-dynamic range image.⁶

Structural information averaged over longer length scales can be obtained from TEM diffraction patterns. Small displacements away from the lattice-defined atomic positions, due to thermal oscillations or lattice distortions, alter the diffraction peak intensities from those

predicted by the scattering factor. This is usually encompassed in the Debye-Waller factor which modifies the scattering factor by a term exponentially dependent on the mean square atomic displacements from their equilibrium positions. Analysis of diffraction peak intensities can thus provide a comparatively simple method for quantifying disorder in the lattice. Figure S2a shows a diffraction pattern from graphene, acquired over an extended dynamic range (see Methods). A hexagonal array of spots is observed, with spacings and intensities consistent with monolayer graphene. Similar patterns were observed for the functionalised graphenes, confirming the retention of long-range order in the carbon lattice.⁷ The average peak intensities for peaks of increasing order is plotted in Figure S2b. To aid comparison, the intensity of orders labelled in red in panel (a) has been reduced by a factor of four because they are stronger reflections caused by constructive interference from the two sub-lattices of graphene.⁸ For graphene at normal incidence, the electron diffraction peak intensities for peaks at reciprocal lattice vector \mathbf{G} can be described by⁸

$$I(G) = A \frac{e^{-2W}}{\delta^4(\mu^2 + G^2)} |S|^2,$$

where δ is the carbon-carbon bond length, S is the relative structure factor (4 for the strong peaks and 1 for the weak peaks), and the Debye-Waller exponent $2W = G^2 u_p^2$. The free parameters are: A , a scale factor that includes microscope dependent parameters; μ the inverse screening length, and u_p the in-plane mean square displacement of the carbon atoms from their usual lattice sites. This mean-square displacement was extracted from fits to the peak intensities for each functionalised sample, and the results are plotted in Figure S2c.

For graphene, the mean square displacement is found to be $u_p = 8 \pm 1$ pm, consistent with a previous report which found $u_p = 6.3 \pm 0.8$ pm.⁸ Note that this mean square displacement is interpreted as the average in-plane displacement of carbon atoms from their ideal lattice positions; distortions in the lattice due to local strain around vacancies and ETDs contribute

to this displacement. Although it is not possible to quantify the concentration of ETDs from the value of the mean displacement alone, an increase in u_p is expected with increasing concentrations of ETDs, giving a convenient signature of increasing disorder in the graphene lattice. After dosing for 30 seconds with atomic oxygen, the mean square displacement has increased to $u_p = 11 \pm 1$ pm, and after 6 min dosing a further increase is seen to $u_p = 13.3 \pm 0.3$ pm. The atomic disorder is similar in GO, with $u_p = 13.9 \pm 0.6$ pm, with a small decrease upon reduction to $u_p = 11.9 \pm 0.2$ pm. This, consistent with the acTEM images, could be associated with a slight increase in lattice order upon reduction. However, the value has not returned to that of pristine graphene, and so, as before, it suggests the reduction treatment alone has not removed the disorder in the lattice.

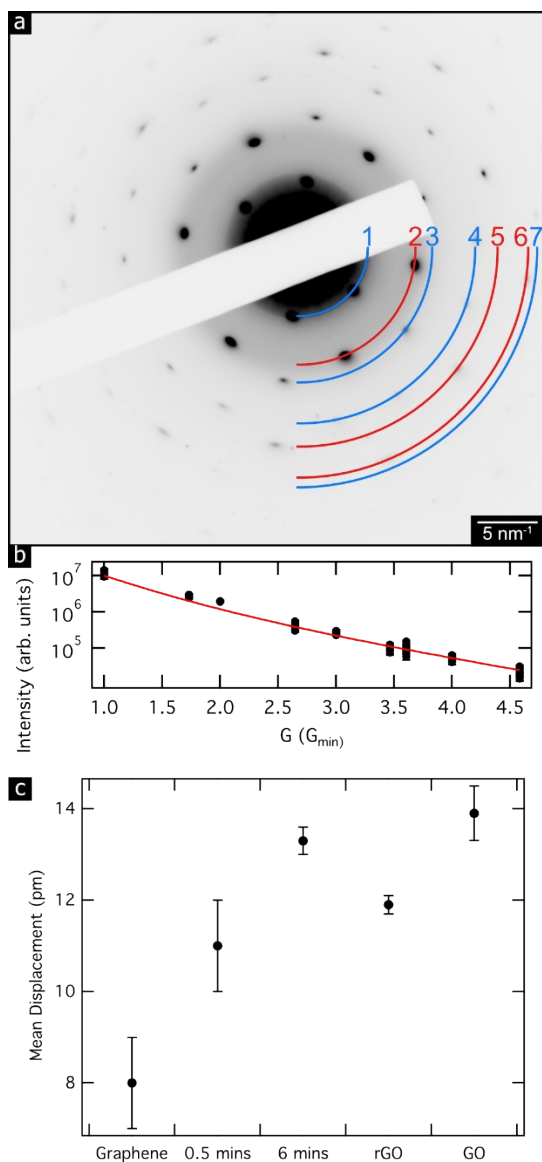


Figure S2. Atomic displacements in graphene measured by electron diffraction. (a) Selected area electron diffraction of CVD grown graphene. Successive orders of diffraction peaks are labelled alongside the blue and red lines. Red corresponds to strong reflections and blue to weak. (b) Intensity of the peaks plotted on a logarithmic scale plotted as a function of the reciprocal vector length in units of the smallest reciprocal lattice vector, the strong reflections have been decreased in intensity by a factor of 4. The red line is a fit to the data using the equation in the text, from which the mean displacement is extracted. (c) The mean displacement of graphene and functionalised graphene, 0.5 mins and 6 mins correspond to the exposure time to atomic oxygen.

ESI3: Molecular Dynamics Simulations

Model Justification

Topological defects such as Stone-Wales defects or grain boundaries are anticipated to form rarely, if at all, on the timescale and temperature scales of these types of simulations, and because of this, the study of their formation and evolution via molecular simulation approaches has thus far been limited. Even in the case of vacancy defects, which can develop on timescales that are practically accessible using ReaxFF simulations, the simulation conditions that are required to accelerate this process are harsh. While this does allow for evaluation of the evolution of graphene functionalization on a timescale accessible to simulation, it is challenging to assess how defects affect oxygen evolution. In such simulations much of the oxygen is lost during the development of vacancy defects, and this limits opportunities to study the interplay between vacancies (or more generally, ETDs) and oxygen groups during annealing. Inducing the formation of both ETDs and oxidative groups prior to annealing enables the study of the interaction between these two types of defect, which are thought to co-exist prior to annealing, on timescales that are amenable to ReaxFF simulations.

To elaborate, the formation energy for a Stone-Wales defect on a carbon nanotube ranges from 4.20 eV to 5.9 eV depending on the curvature of the tube, according to calculations performed using a continuum model.⁹ While extending this formalism to graphene oxide would be prohibitively complex, these formation energies can give some indication of the barrier for formation on graphene oxide, though we expect the energy to be lower in the presence of oxygen. Even at our highest temperature of 2500K, 4.2 eV is still 20 times greater than $k_B T$, and thus unlikely to be overcome by thermal energy alone. Thus, in order to

study the influence of topological defects quantitatively, we need to introduce them into our initial structures. This concept is supported by our own simulations and from previous simulations of graphene oxide. While not explicitly discussed, in viewing previously reported graphene oxide structures from various simulations post-annealing, we did not observe Stone-Wales defects arise in most simulations despite a range of annealing schedules and temperatures, even up to 5000 K.¹⁰⁻¹⁴ Perhaps due to a slower heating schedule, Liu et al. did report a structure which results in two Stone-Wales defects after annealing at 1500K,¹⁵ but this low number of defects is still not sufficient for studying oxygen evolution on topological defects quantitatively.

Figures and Tables

Table S1. Percentage of carbon atoms ejected from the GO surface compared to the initial total number of carbon atoms with no defects (GO-N), with vacancy defects (GO-V), with topological defects (GO-T) and with both vacancy and topological defects (GO-TV) after annealing at 300K, 600K, 900K, 1200K and 2500K. No number reported is equivalent to zero carbons ejected, and 0.0 is equivalent to a non-zero number of carbons less than 0.05%.

	Replica	300	600	900	1200	2500
GO-N	1				0.0	0.6
	2					0.4
	3					0.3
GO-V	1			0.1	0.2	1.1
	2				0.2	0.9
	3				0.2	1.3
GO-T	1				0.1	1.3
	2		0.0	0.0	0.2	0.8
	3				0.1	1.5
GO-TV	1				0.1	1.9
	2			0.1	0.2	1.7
	3				0.1	1.3

Table S2. Location of post-annealing retained oxygen atoms on the GO surface for initial structures with no defects (GO-N), vacancy defects (GO-V), topological defects (GO-T) and with both vacancy and topological defects (GO-TV) after annealing at 300K, 600K, 900K, 1200K and 2500K. Defect oxygens are defined as those bound to defect carbons. Basal oxygens are defined as those bound to the basal plane. Bound oxygens are defined as the total amount of oxygens retained on the surface. Data are reported as the absolute number of oxygen atoms (expressed as a percent of the total number of bound oxygens in parentheses).

	O Type	600	900	1200	2500
GO-N	Defect	5 (3±2)	17 (12±6)	25 (32±7)	10 (97±4)
	Basal	187 (97±2)	122 (88±6)	51 (68±7)	0 (3±4)
	Bound	192 (64±1)	139 (47±3)	76 (25±5)	10 (3±1)
GO-V	Defect	50 (24±3)	53 (32±4)	45 (41±3)	32 (91±7)
	Basal	160 (76±3)	112 (68±4)	66 (59±3)	3 (9±7)
	Bound	210 (70±2)	164 (55±4)	112 (37±2)	36 (12±0.4)
GO-T	Defect	120 (55±3)	111 (62±2)	99 (79±5)	18 (97±4)
	Basal	99 (45±3)	69 (38±2)	26 (21±5)	1 (3±4)
	Bound	219 (73±1)	180 (60±3)	125 (42±1)	19 (6±1)
GO-TV	Defect	108 (48±4)	124 (61±3)	102 (76±2)	29 (100±0)
	Basal	117 (52±4)	78 (39±3)	33 (24±2)	0 (0±0)
	Bound	226 (75±1)	202 (68±1)	135 (45±2)	29 (10±1)

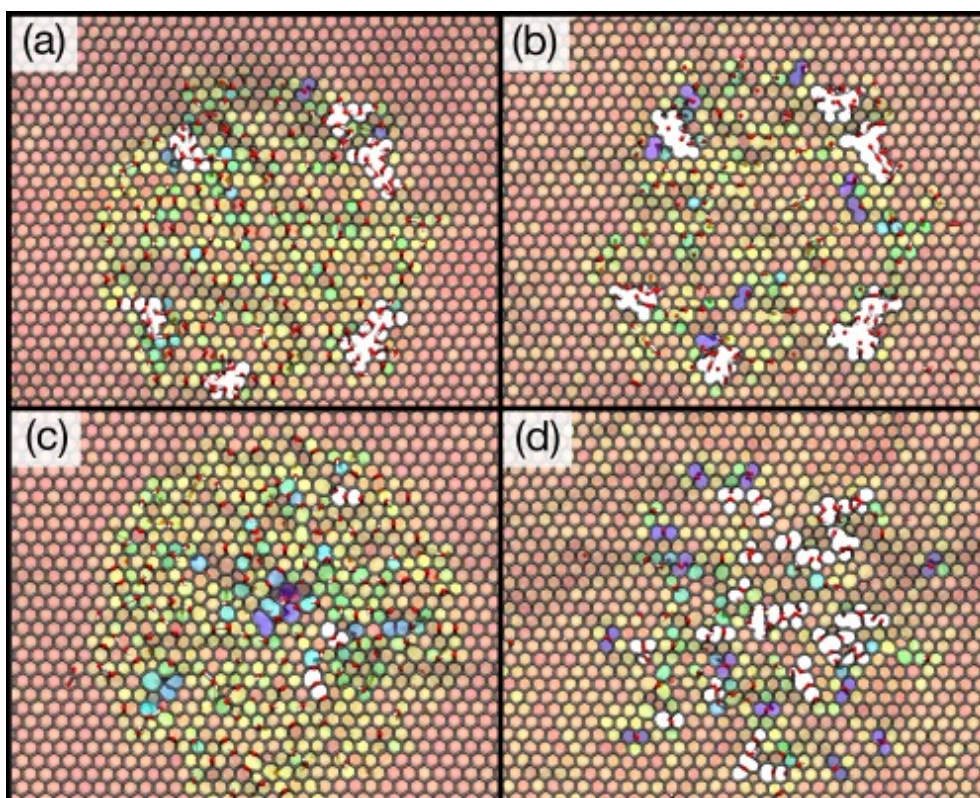


Figure S3. Top-down view of post-annealed graphene oxide sheets with vacancy defects introduced (GO-V) after annealing at (a) 300K and (b) 1200K and with topological defects introduced (GO-T) after annealing at (c) 300K and (d) 1200K. Carbon atoms are represented as grey, oxygen atoms are red, and hydrogen atoms are white. Space-filling colours represent ring pucker from unstrained (red) to strained (violet). White space represents vacancy defects.

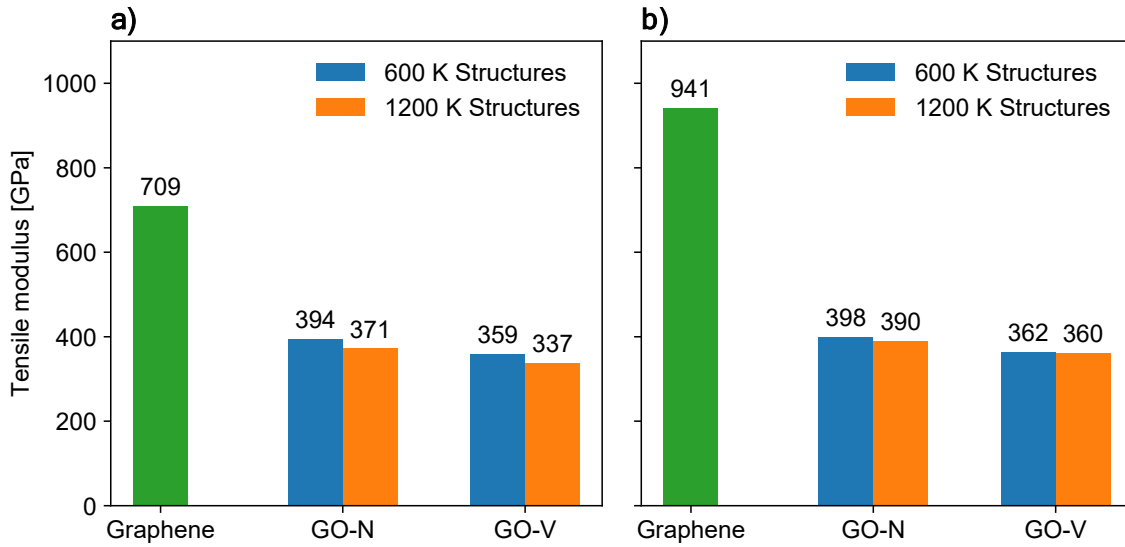


Figure S4. Summary of calculated Young's modulus, E , (GPa) of post-annealing GO samples (annealed at 600 K and 1200 K) with no initial vacancies (GO-N) and GO samples with initial vacancy defects (GO-V), compared with pristine graphene. Panel a) shows values calculated via finite temperature stress-strain approach which was performed at 300K, and panel b) presents values calculated via the elastic constants approach. To calculate the 2D Young's modulus, sheet thicknesses of 3.3 Å, 5.86 Å and 6.24 Å for graphene, GO-N, and GO-V, respectively, were assumed. Using the stress-strain calculated values, the 2D moduli then become 234 N/m, 231 N/m, 217 N/m, 224 N/m 210 N/m, for graphene, 600 K GO-N, 1200 K GO-N, 600K GO-V, and 1200K GO-V, respectively. Using the calculated values from the elastic constant method, the 2D moduli are 306 N/m, 233 N/m, 228 N/m, 226 N/m, and 225 N/m for graphene, 600 K GO-N, 1200 K GO-N, 600K GO-V, and 1200K GO-V, respectively.

ESI4: Computational Details

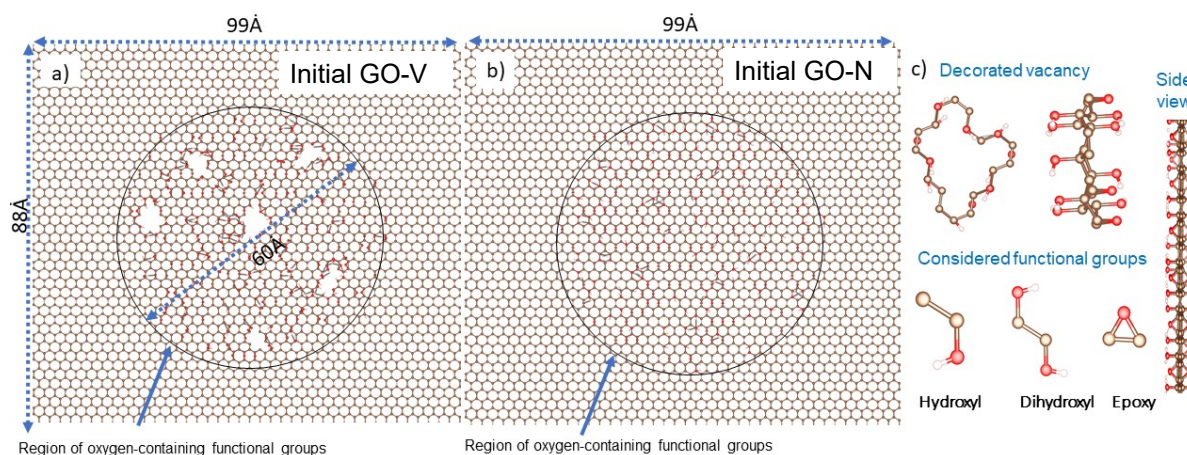


Figure S5. a) Initial structure of GO-V and b) initial structure of GO-N, both with the size and the initial region of oxygen-containing functional groups indicated. c) The geometry of a decorated vacancy, the considered functional groups, and a side view of one example structure. Carbon atoms are shown in pink, oxygen atoms in red, and hydrogen atoms in white.

In all models (GO-N, GO-V, GO-T, GO-TV) oxygen functional groups were added to an initial circular region of radius 60 Å as indicated in Figure S5. The groups added were hydroxyl, dihydroxyl, and epoxide, in a ratio of 1:1 for overall hydroxyls to epoxide, and 7:3 for dihydroxyl:hydroxyl. Dihydroxyls were defined as two hydroxyls added adjacent to one another located on opposite sides of the sheet, as shown in Figure S5c. The functional groups were added in spatially randomised locations within the circular region either above or below the sheet, with an equal number added to either side.

For the study of vacancy defects (GO-V), six holes in the carbon lattice were created via the removal of 10, 7, 5, 5, 5 and 3 carbon atoms, as discussed in the main manuscript. For the study of topological defects (GO-T), 16 Stone-Wales defects were introduced, along with one “miniature”-grain boundary. Stone-wales defects were introduced through randomly selecting two bonded atoms within the circular region and applying a 90° rotation to the bond, resulting in a Stone-Wales patch. For the grain boundary, a 24-atom selection was rotated by 90°, resulting in six 5-membered rings and six 7-membered rings. To allow for

more complex topology, Stone-Wales defects were allowed to border one another (for example, one 7-membered ring could border another 7-membered ring), although the central two atoms (or 24 atoms for the grain boundary defect) could not participate in more than one rotation.

For the study of both vacancy and topological defects combined (GO-TV), the same initial carbon lattices from GO-V were used, and topological defects (eight Stone-Wales and one “mini”-grain boundary) were introduced bordering these vacancies.

Functional Group Analysis

To analyse the post-annealing distribution of functional groups, retained oxygen atoms were categorized based on their environment. Groups considered were epoxide, ether (the non-epoxide ether groups), carboxylic acid, hydroxyl, and carbonyl. All other groups were in the minority as trace groups and not further considered. Bond distance cut-offs used for determining nearest neighbours were 1.2 Å, 1.8 Å, 1.8 Å, 1.5 Å and 1.1 Å for O-H, C-C, O-C, O-O and H-H bonds, respectively. A group was considered to be attached to the GO sheet (“bound”) if the neighbouring bonded carbon has at least one carbon neighbour. Carboxylic groups were counted prior to counting hydroxyls and carbonyls, to ensure these groups were not double counted. Similarly, di-hydroxyls were counted prior to counting hydroxyls. In Figure 4 (main text), the category “Ether” included both epoxide and non-epoxide ether groups (where the two carbons were too distant to be considered as bonded).

Rendering Methods

VMD was used for the visualisation of defects in both Figures 2, 3, and Figure S3. In Figure 2, a space filled colouring of the carbon lattice was used to visualise topological defects in the graphene ring network. Ring network topology was characterized via the shortest path method¹⁶ using a carbon-carbon bond cut-off of 1.85 Å and was calculated using only carbon

atoms. The rings were then coloured according to the ring size; 5-member: blue, 6-member: grey, 7-member: yellow, 8-member: green, 9-member: pink, >9: white. No stable three- or four-member rings were observed. Oxygen atoms were then overlaid using the CPK representation, such that oxygen atoms on either side of the carbon lattice are visible.

In Figure 3, example defects were chosen by visual inspection and rendered using CPK for atoms and DynamicBonds for bonds with a bond cut-off of 1.8 Å. In Figure S3 CPK and DynamicBonds was used as in Figure 3, but additionally the PaperChain drawing method¹⁷ was used to colour the carbon lattice by ring pucker¹⁸ with a maximum ring size of 10. Ring pucker gives an indication of the distortion of a ring, and thus provides a method of qualitatively visualizing the distortion within the GO sheet.

Mechanical Property Calculations

The stress-strain curves of the GO sheets under tensile (planar) deformation at finite temperature were calculated via MD simulations by increasing the simulation cell size along one of the two principal lateral axes (either in the x - or y -direction). The GO sheet structures used for these simulations was taken from the last frame of the trajectory from the relevant heating process. This frame was then subjected to relaxation via 10 ps of NPT simulation at 300 K. Following this, the sample was subjected to tensile strain at the same temperature in the NPT ensemble, with the strain rate was set constant at a value of 10^{-5} fs^{-1} . Young's modulus was obtained as $E = d\sigma_{ii}/d\epsilon_i$ for the linearized portion of the stress-strain curve, which was determined from the part of the stress-strain curve up to 0.75% strain, where ii is the component of the virial tensor stress and i is the strain along the axial direction ($=x$ or y). The Young's moduli presented in the Supplementary Results section (Figure S4) represent the average of the values calculated along the two principal lateral directions.

The elastic constants of the GO sheets were also calculated at 0 K at a constant pressure,¹⁹ which can be defined as the second derivative of the total potential energy (U), with respect to small strain deformations (ε_i)^{20,21} as shown in Equation 1:

$$C_{ij} = \frac{1}{V} \left(\frac{\partial^2 U}{\partial \varepsilon_i \partial \varepsilon_j} \right) \quad (1)$$

where V is the volume of the simulation cell, and i and j correspond here to the so-called contracted rating and have values ranging from 1 to 6. Using LAMMPS, the calculation of elastic constants at 0 K was performed using the energy minimization method, with the GO structures obtained from the MD simulations used as input. In these calculations, only the configuration information of the GO structure is taken into account. To compute Young's modulus (E) using the stiffness matrix C , the isotropic properties of the GO sheets were checked *via* the relation proposed by Zener, according to which the isotropy, a_T , of the material is expressed as provided in Equation 2:

$$a_T = \frac{2C_{44}}{C_{11} - C_{12}} \sim 1 \quad (2)$$

This means that in an isotropic medium, there are only two independent elastic constants to express the different mechanical properties such as Young's modulus (E), which can be obtained using Equation 3:

$$E = \frac{\mu(2\mu + 3\lambda)}{\lambda + \mu} \quad (3)$$

where the two Lamé constants are expressed as $\mu = C_{44}$ and $\lambda = C_{12}$.

ESI5: Measuring mechanical properties by atomic force microscopy

All AFM data were acquired using an Asylum Research MFP3D-SA AFM with MikroMasch NSC18 tips (silicon tip with nominal normal spring constant of 2.8 Nm^{-1} , resonance frequency of 75 kHz, and tip radius of 8 nm) which were calibrated using the Sader method.²² The graphene, or functionalised graphene, was suspended across circular holes with diameters of $3.25 \mu\text{m}$ in a silicon nitride support membrane. The centre of each hole was found by imaging in AC mode (tapping mode), see Figure S6, and force-distance curves acquired at the centre point. The force-distance curves were acquired with sequentially increasing maximum load force until the membrane was observed to break. The breaking load was determined from the highest load reached before breaking. Figure S7 gives examples of breaking curves captured on graphene and functionalised graphene.

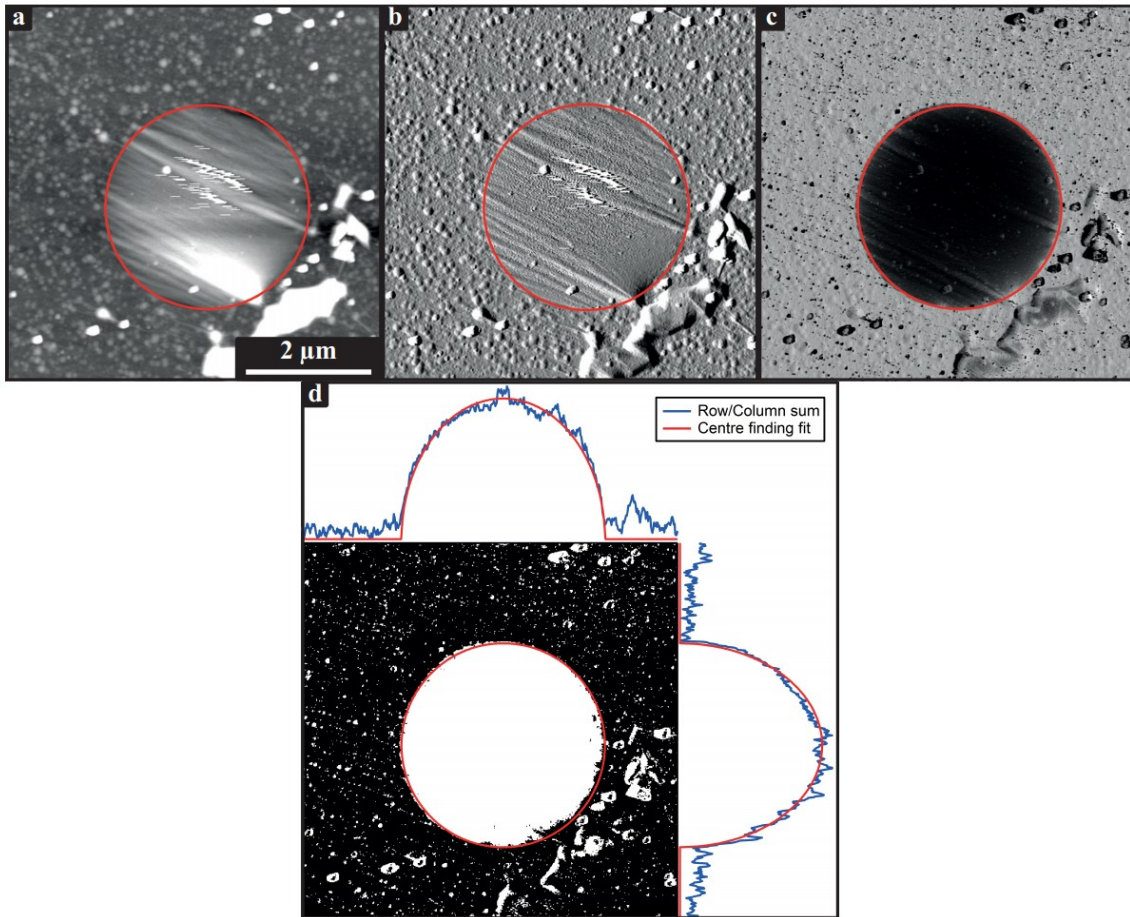


Figure S6. Tapping mode AFM image of a graphene covered hole. The channels and their corresponding data scales are a) height, 35 nm, b) amplitude, 5 nm with a minimum value of 35 nm, c) phase, 60° with a minimum value of 75°. d) Thresholded version of c) with summed rows and columns. The location of the hole is found by the fitting as highlighted by a red circle in all images.

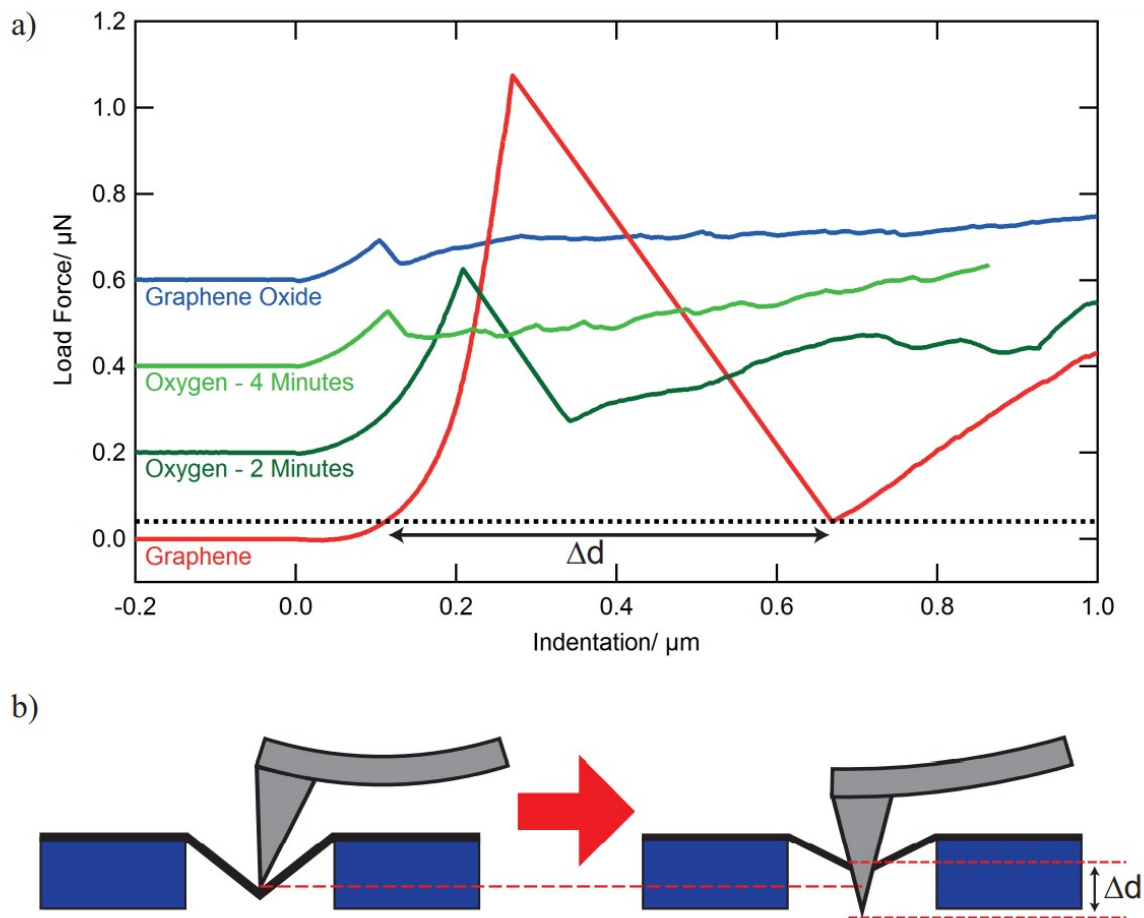


Figure S7. a) Force versus indentation curves for different levels of oxygen functionalisation, showing the differences in the breaking behaviour. The curves have been offset to make them easier to distinguish — the left flat section of each corresponds to a load force of 0 N. b) Schematic of a break event as seen from the side in a cross-sectional view, showing the change in indentation, Δd . Schematic is not to scale.

Force-distance curves from the approach direction up to the breaking point were transformed to force versus indentation and corrected for offsets. The resultant force versus indentation curve was fit to extract the 2D elastic modulus and pretension of the membrane. An example curve with corresponding fit is given in Figure S8.

To explain the force versus indentation behaviour we use a simple mechanical model that has previously been used to determine the mechanical properties of graphene from indentation of a circular suspended membrane.²³ Provided the radius of the AFM tip is significantly smaller than the radius of the hole ($r_{tip} \ll r_{hole}$) and acting close to the centre of

the hole, the system can be modelled as a point load acting on a clamped circular membrane of linear (i.e. no bending stiffness) isotropic elastic material. This model can be used to approximate the force-indentation (F - d) relationship as

$$F = \sigma_{2D}^0(2\pi r_{hole})\left(\frac{d}{2r_{hole}}\right) + E_{2D}(2q^3 r_{hole})\left(\frac{d}{2r_{hole}}\right)^3,$$

where σ_{2D}^0 is the pretension and E_{2D} is the 2D elastic modulus. E_{2D} is analogous to the Young's modulus of a 3D material and can be converted to an equivalent Young's modulus by dividing by the thickness of the sheet — for graphene the interplanar distance of graphite, 0.335 nm, was used and this is plotted in Figure 5 along with the 2D elastic modulus. Note that the layer thickness increases in GO and is typically taken to be around 1 nm. The dimensionless parameter, q , is given by $q = (1.05 - 0.15\nu - 0.16\nu^2)^{-1}$, where ν is the Poisson ratio. For graphene the Poisson ratio can be taken as the in-plane Poisson ratio for graphite, 0.165, giving $q = 1.02$.

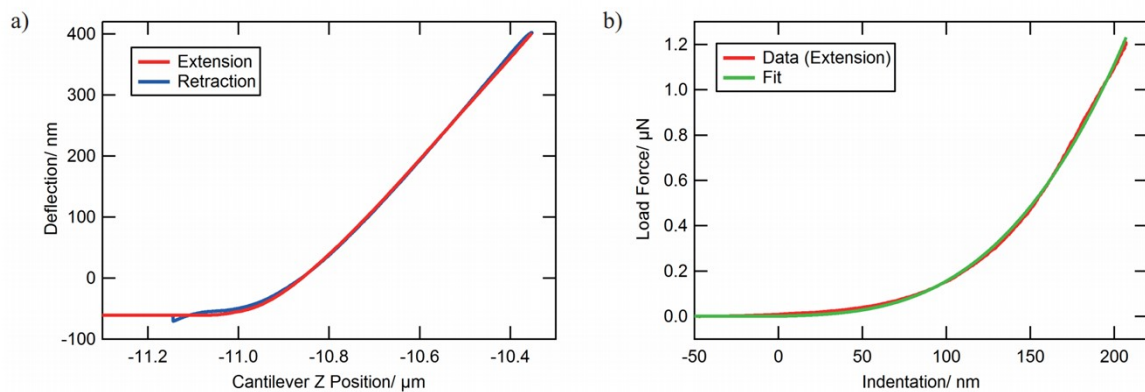


Figure S8. Example force curve from a graphene covered hole. a) Deflection versus z position of the cantilever. b) Force versus indentation, with fitting of equation 3.1. The force was zeroed using the flat section of the curves (which extends far to the left of both (a) and (b)) before fitting and the indentation was zeroed after fitting using the fitted offset parameter.

REFERENCES:

- 1 S. Doniach and M. Sunjic, Many-electron singularity in X-ray photoemission and X-ray line spectra from metals, *J. Phys. C Solid State Phys.*, 1970, **3**, 285–291.
- 2 A. J. Marsden, M.-C. M.-C. Asensio, J. Avila, P. Dudin, A. Barinov, P. Moras, P. M. Sheverdyeva, T. W. White, I. Maskery, G. Costantini, N. R. Wilson and G. R. Bell, Is graphene on copper doped?, *Phys. status solidi - Rapid Res. Lett.*, 2013, **7**, 643–646.
- 3 A. J. Marsden, P. Brommer, J. J. Mudd, M. A. Dyson, R. Cook, M. Asensio, J. Avila, A. Levy, J. Sloan, D. Quigley, G. R. Bell and N. R. Wilson, Effect of oxygen and nitrogen functionalization on the physical and electronic structure of graphene, *Nano Res.*, 2015, **8**, 2620–2635.
- 4 K. Chenoweth, A. C. T. van Duin, W. A. Goddard, O. Seri-Livni, C. Saguy, F. Horani, E. Lifshitz, D. Cheskis, R. Smith, K. Jolley, C. Latham, M. Heggie, A. C. T. van Duin, D. van Duin, H. Wu, S. Plimpton, A. C. T. van Duin, S. Dasgupta, F. Lorant, W. A. Goddard, A. C. Ferrari, D. M. Basko, B. Shevitski, M. Mecklenburg, W. A. Hubbard, E. R. White, B. Dawson, M. S. Lodge, M. Ishigami, B. C. Regan, S. H. Dave, C. Gong, A. W. Robertson, J. H. Warner, C. Grossman, M. M. Z. Hossain, J. E. J. Johns, K. H. K. K. H. Bevan, H. J. Karmel, Y. T. Liang, S. Yoshimoto, K. Mukai, T. Koitaya, J. Yoshinobu, M. Kawai, A. M. Lear, L. L. Kesmodel, S. L. Tait, M. C. Hersam, J. C. Meyer, R. S. Sundaram, A. Chuvilin, S. Kurasch, M. Burghard, K. Kern, U. Kaiser, P. Feicht and S. Eigler, Chemically homogeneous and thermally reversible oxidation of epitaxial graphene., *Nat. Chem.*, 2012, **4**, 305–9.
- 5 A. C. Ferrari and D. M. Basko, Raman spectroscopy as a versatile tool for studying the properties of graphene, *Nat. Nanotechnol.*, 2013, **8**, 235–246.
- 6 K. Evans and R. Beanland, High Dynamic Range Electron Imaging: The New Standard, *Microsc. Microanal.*, 2014, **20**, 1601–1604.

- 7 N. R. Wilson, P. A. Pandey, R. Beanland, R. J. Young, I. A. Kinloch, L. Gong, Z. Liu, K. Suenaga, J. P. Rourke, S. J. York and J. Sloan, Graphene Oxide: Structural Analysis and Application as a Highly Transparent Support for Electron Microscopy, *ACS Nano*, 2009, **3**, 2547–2556.
- 8 B. Shevitski, M. Mecklenburg, W. A. Hubbard, E. R. White, B. Dawson, M. S. Lodge, M. Ishigami and B. C. Regan, Dark-field transmission electron microscopy and the Debye-Waller factor of graphene, *Phys. Rev. B*, 2013, **87**, 045417.
- 9 E. Ertekin, D. C. Chrzan and M. S. Daw, Topological description of the Stone-Wales defect formation energy in carbon nanotubes and graphene, *Phys. Rev. B*, 2009, **79**, 155421.
- 10 A. Bagri, C. Mattevi, M. Acik, Y. J. Chabal, M. Chhowalla and V. B. Shenoy, Structural evolution during the reduction of chemically derived graphene oxide, *Nat. Chem.*, 2010, **2**, 581–587.
- 11 L.-C. C. Lin and J. C. Grossman, Atomistic understandings of reduced graphene oxide as an ultrathin-film nanoporous membrane for separations, *Nat. Commun.*, 2015, **6**, 8335.
- 12 A. Antidormi, S. Roche and L. Colombo, Impact of oxidation morphology on reduced graphene oxides upon thermal annealing, *J. Phys. Mater.*, 2019, **3**, 015011.
- 13 Z. Yang, Y. Sun, F. Ma, Y. Lu and T. Zhao, Pyrolysis mechanisms of graphene oxide revealed by ReaxFF molecular dynamics simulation, *Appl. Surf. Sci.*, 2020, **509**, 145247.
- 14 F. Raffone, F. Savazzi and G. Cicero, Molecular dynamics study of the pore formation in single layer graphene oxide by a thermal reduction process, *Phys. Chem. Chem. Phys.*, 2021, **23**, 11831–11836.
- 15 X. Liu and Q. Yang, Molecular dynamic simulation of mechanical behaviour of RGO

- produced by thermal reduction method, *Micro Nano Lett.*, 2017, **12**, 638–642.
- 16 D. S. Franzblau, Computation of ring statistics for network models of solids, *Phys. Rev. B*, 1991, **44**, 4925–4930.
- 17 S. Cross, M. M. Kuttel, J. E. Stone and J. E. Gain, Visualisation of cyclic and multi-branched molecules with VMD, *J. Mol. Graph. Model.*, 2009, **28**, 131–139.
- 18 D. Cremer and J. A. Pople, General definition of ring puckering coordinates, *J. Am. Chem. Soc.*, 1975, **97**, 1354–1358.
- 19 W. G. Hoover, Canonical dynamics: Equilibrium phase-space distributions, *Phys. Rev. A*, 1985, **31**, 1695–1697.
- 20 H. Jabraoui, Y. Vaills, A. Hasnaoui, M. Badawi and S. Ouaskit, Effect of Sodium Oxide Modifier on Structural and Elastic Properties of Silicate Glass, *J. Phys. Chem. B*, 2016, **120**, 13193–13205.
- 21 A. Pedone, G. Malavasi, M. C. Menziani, U. Segre and A. N. Cormack, Role of Magnesium in Soda-Lime Glasses: Insight into Structural, Transport, and Mechanical Properties through Computer Simulations, *J. Phys. Chem. C*, 2008, **112**, 11034–11041.
- 22 J. E. Sader, J. W. M. Chon and P. Mulvaney, Calibration of rectangular atomic force microscope cantilevers, *Rev. Sci. Instrum.*, 1999, **70**, 3967–3969.
- 23 C. Lee, X. Wei, J. W. Kysar and J. Hone, Measurement of the Elastic Properties and Intrinsic Strength of Monolayer Graphene, *Science (80-.)*, 2008, **321**, 385–388.